Metal Chalcogenide Nanotubes

W. Tremel, H.A. Therese, N. Zink, M.N. Tahir, I. Shukoor,
Institut für Anorganische Chemie Chemie, Johannes Gutenberg-Universität,
Duesbergweg 10-14, D-55099 Mainz (Germany)
U. Kolb
Institut für Physikalische Chemie, Johannes Gutenberg-Universität,
Welderweg 11, D-55099 Mainz (Germany)
G. Schönhense, H.J. Elmers
Institut für Physik, Johannes Gutenberg-Universität,
Staudingerweg 7, D-55099 Mainz (Germany)

After the discovery of carbon fullerenes and nanotubes about a decade ago it became clear that polyhedral structures are the thermodynamically stable form of carbon under the condition that the number of carbon atoms is limited. When we analyze the physicochemical reasons for the formation of nanostructures we recognize that curved nanostructures are in no way restricted to carbon. The large energy of the "dangling bonds" at the periphery of these nanoparticles is responsible for the pronounced formation tendency of carbon fullerenes and nanotubes. However, the same should apply for inorganic compounds (BN,[1] MQ_2 (M = Ti, V, Mo. W. Re; Q = S, Se),[2] MI_2 [3] or V_2O_5 [4]) as well. During the past years this hypothesis was substantiated by numerous examples and it can be safely assumed that the phase diagrams of elements which form layered compounds contain fullerene- and nanotube-like structures.

Under the condition that particles of these layered systems are not larger that 200 nm, curved nanostructured may form as thermodynamically stable phases. Nanotubes have also been obtained from typical 3D-compounds such as TiO_2. Therefore there seems to be no restriction for the formation of nanostructures. However, it is immediately apparent that 3D structures cannot form perfect nanostructures because many bonds at the surface of the aggregates remain unsaturated. Layer compounds, however, are able to form perfectly crystallized pore and tube structures. It seems reasonable that these structures are formed during the nucleation period. Therefore the intrinsic nucleation barriers for the phases are small.

Synthesis of chalcogenide nanoparticles

Various strategies have been developed to prepare nanostructured metal chalcogenides including sulfides and selenides through different growth mechanisms. A characteristic feature of all closed-shell structures is that high reaction temperatures (> 800°C) or large activation energies are needed to overcome the activation barrier associated with the bending of the otherwise flat 2D layers.[16] Fullerene-like structures of the Mo and W sulfides and selenides have been prepared by the reaction of the oxides with H_2S (H_2Se) and H_2 and N_2 at elevated temperatures. [5, 6] High energetic techniques that can provide large activation energies in a very short period, such as electron irradiation, [7] laser ablation, [8] microwave plasma, [9] arc discharge, [10] and pulsed laser vaporization, [11] have been used to synthesize a variety of IF- like nanostructures. Schuffenhauer et al.[12] have synthesized nested fullerene-like NbS_2 by the reaction between $NbCl_5$ vapour and H_2S gas at 400°C followed by further heat treatment at 550°C.

As the above methods have to rely mostly on high temperatures and/or complicated processes they may not be optimally suited for a large-scale preparation of nanostructured

metal chalcogenides with a minimum amount of side products. On the other hand, as the mechanical, physical and catalytic properties of nanostructured chalcogenides strongly depend on their size and shape, it is desirable to devise synthetic procedures that enable us to control the particle size and morphology to a significant extent. From an application point of view, the focus on nanoparticle growth will be on high purity, high-yield and therefore low-cost products. We report here on new approaches in nanoparticle synthesis and functionalization made by the solid state group in Mainz.

MOCVD synthesis. We have devised a facile and large scale synthesis for well defined MoS_2 and $MoSe_2$ nanoparticles, by heating the precursors obtained from a metal organic chemical vapor deposition (MOCVD) approach, where $Mo(CO)_6$ and elemental sulfur or selenium were used as starting materials. Initial exploratory experiments indicated that the particle diameters can be controlled by the reaction temperature. In the case of MoS_2, reactions at 350°C lead to the formation of agglomerated particles with diameters between 10 and 40 nm. By further increasing the reaction temperature to 450°C we obtained nanoparticles with diameters between 10 and 30 nm which showed partial agglomeration. The electron diffraction patterns of those particles revealed very diffuse rings indicative of a weak long range order. Scanning electron micrographs of the black colored molybdenum sulfide and molybdenum selenide samples obtained from the MOCVD processes (MOCVD sample) are shown in Figure1. The SEM images show that the MOCVD samples contain nanoparticles of unique morphology. The morphology of the samples was studied further by transmission electron microscopy (TEM).
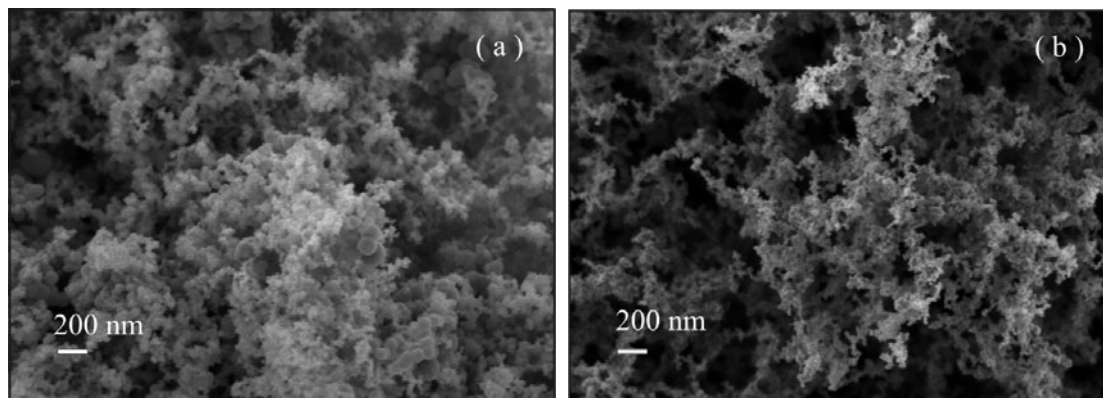

Figure 1. SEM images of the MoS_2 (a) and $MoSe_2$ (b) nanoparticles obtained from the MOCVD processes at 450°C and 500°C respectively.

The MoS_2 sample contains particles in the size range between 5 and 20 nm. Each particle is made up of amorphous components (Figure 2, circled in Figure 2c) and irregularly shaped S-Mo-S nanolayers. Most of these layers are curved, and one such pair of curved layers is marked in Figure 2c. The interlayer d-spacing was calculated to be 0.70 nm, which is larger than the (002) d-spacing of 0.64 nm in $2H-MoS_2$. The increased d-spacing can be attributed to the curved structure of the nanoparticles. The particles appear te be sintered together. Similarly, TEM images of $MoSe_2$ also show more of shorter and curved lattice fringes (see Fig 2d). The d-spacing between the lattice fringes is 0.62 nm, which is closer to the separation of the (002) planes of hexagonal $MoSe_2$. The x-ray diffraction patterns of the MOCVD samples show very broad reflections, indicating that the products obtained from the MOCVD step have short range structural order and smaller particle sizes.
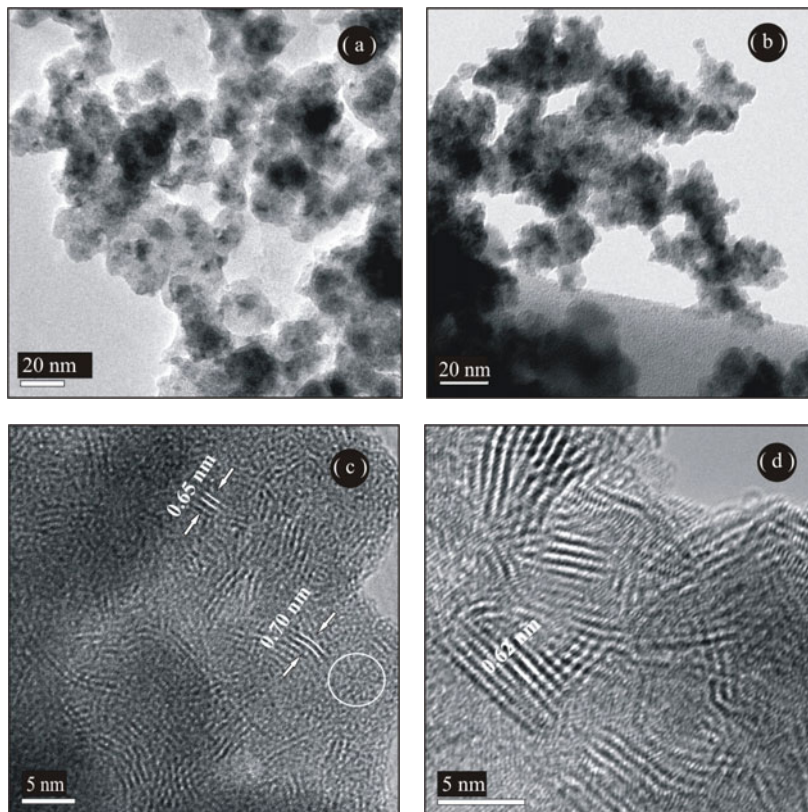
Figure 2. TEM images of the MoS$_2$ ((a),(c)) and MoSe$_2$ ((b),(d)) obtained from the reactions carried at 450°C and 500°C respectively.

The explanation for the formation of the monodispersed nanoparticles at temperatures close to 450/500°C is that by the evaporation of S/Se and the thermal decomposition of Mo(CO)$_6$ MoQ$_2$ nuclei are formed in the gas phase. As S/Se is vaporized completely at this temperature and only small nucleation clusters are present in the gas phase, no sample inhomogeneities resulting from Mo or S/Se grains are observed. Since the growth of the MoQ$_2$ particles during the MOCVD step is limited by the quenching at the graphite receptor, the nanoparticles shown in Figure 2 represent the kinetic product distribution in the gas phase at 450°C approximately 5 min after the reaction of Mo(CO)$_6$ and S$_8$/Se$_8$. As a minimum particle size is required for the formation of onion or nanotube-type structures, only particles containing sheet-like lamellae are found. A subsequent growth step has to be added where the lamellar sheet fragments continue to grow and begin to loosen at their ends until they roll up into separate scrolls. Smaller sheet fragments will form onion-type structures, whereas larger sheets may form scrolls or tubes. This growth process may be initiated by heating the graphite receptor or the reaction chamber of the MOCVD reactor or by a subsequent heat treatment of the MoQ$_2$ nanoparticles. Therefore, a series of experiments have been conducted to obtain a better understanding of the growth process.

Particle growth. As it is known that the closed caged structures are thermodynamically more stable than their isolated lamella-like structures at higher temperatures, the influence of the temperature on the MOCVD samples was studied at different temperature. During these studies the temperature range between 700 and 800°C proved to be most relevant. Figure 3 shows the low resolution TEM images of the heat treated MOCVD samples. The heating increases the ordering within the nanoparticles, and

3

a large quantity of MoS_2 and $MoSe_2$ onions with diameters between 30 nm and 60 nm formed during the heat treatment. MoS_2 yielded fullerene-like particles at 700°C and incompletely closed round particles at 800°C. In contrast, $MoSe_2$ yielded onions only at 800 °C. At 700°C, nanoparticles with diameters between 30 nm and 50 nm with distinctly curved layers, but still partially open were obtained. At 800°C hollow closed spherical particles were formed. By increasing the annealing temperature to 900°C elongated $MoSe_2$ nanoparticles with tube- or rod-like structures were formed. As the precursor obtained from the MOCVD process had already layered motifs, the IF-like particles obtained after heat treatment were completely hollow which is different from the IF-like particles obtained by sulfidization of metal oxide particles reported earlier.[13]
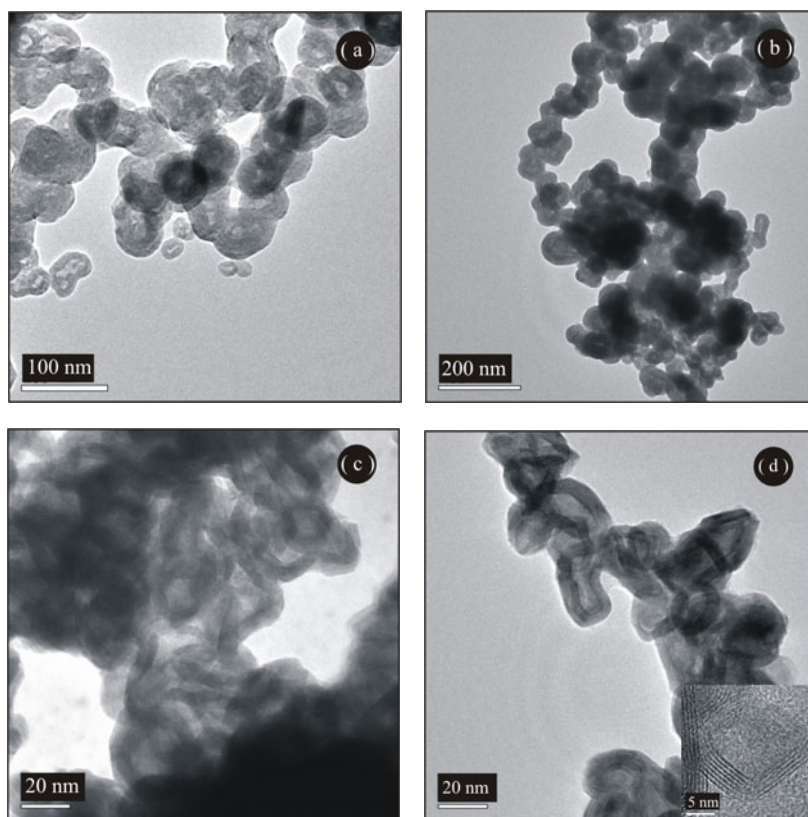

Figure 3. Low resolution TEM micrographs of heat treated MoS_2 at 700°C (a), 800°C (b), and of heat treated $MoSe_2$ at 700°C (c), 800°C (d) for a duration of 1 hr.

The interior part of these nanoparticles shown in Figure 3d contains a number of edge dislocations where layers of $MoSe_2$ sheets are intergrown to yield onions with corner-shaped fragments. These corners may originate from primary $MoSe_2$ sheet fragments which saturate their dangling bonds at the layer edges by intergrowth. However, as the layers would be too severely bent in small spherical $MoSe_2$ particles with diameters of approx. 10 nm, hollow particles are formed by interconnecting sheets of primary particles which leads to corners at the interface of these particles as shown in Figure 3d and the HRTEM image in the inset. Annealing temperatures higher than 700°C leads to enhanced layer growth. The ordering within the onions increases at 800°C and fully crystalline and closed $MoSe_2$ layers are formed after 1hour of annealing time (Figure 4). The fullerene–like particles in Figure 4a and 4d show an average spacing of 0.63 nm and 0.65 nm between their curved layers which is closer to the d-spacing of their corresponding dichalcogenides

with hexagonal modification. The EDX analyses of the fullerene-like particles confirm the presence of Mo and Q (S, Se) in a 1:2 ratio.
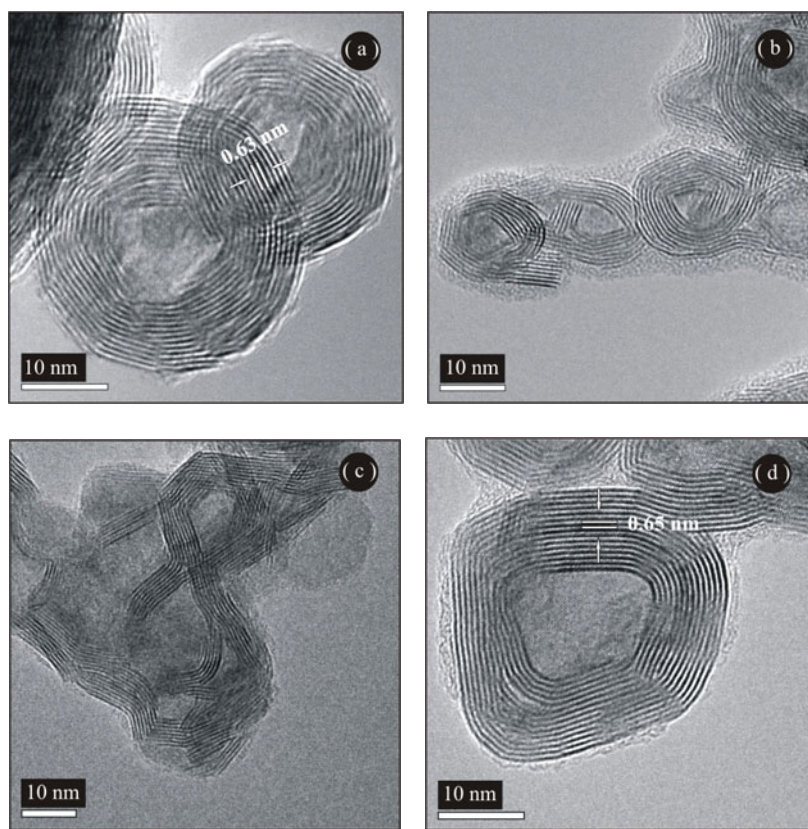

Figure 4. HRTEM micrographs of heat treated MoS_2 at 700°C (a), 800°C (b), and of heat treated $MoSe_2$ at 700°C (c), 800°C (d) for a duration of 1 hr. In (a) and (d) closed and hollow IF MoS_2 and $MoSe_2$ nanoparticles are shown, (b) and (c) show incomplete and partially open MoS_2 (b) and $MoSe_2$ (c) particles.

An *in situ* TEM study of the nanoparticle formation using a TEM heating stage in the temperature range between 500°C and 1000°C revealed that distinct amorphous primary particles shown in Figure 5a lead to different MoS_2 nanoparticles upon heating. While the large particles marked by the dotted circle in Figure 5 transform to massive well ordered IF MoS_2 particles (Figure 5b) above 700°C, the smaller particles marked by the full circle transform hollow MoS_2 particles with no apparent order (Figure 5c). A cautionary note must be added because the results shown in Figure 5 differ to some extent from those presented in Figures 1-4. The IF particles shown in Figure 1-4 were obtained in a conventional tube furnace, whereas the particles depicted in Figure 5 were obtained under UHV condition on a TEM heating stage. Meanwhile, the MOCVD approach has been applied well to WS_2 and WSe_2. Furthermore, the two step process described above can be conducted as a one step process under a suitable choice of conditions.

Sulfide nanoparticles starting from oxide precursors. Oxide nanoparticles, e.g. WO_3 nanorods were found to be a versatile precursor in the synthesis of WS_2 nanotubes which were synthesised by annealing in a H_2S stream a nanostructured tungsten oxide precursor, which was produced by heating tungsten filaments under reduced pressure in the presence of water vapour.[13] Walton and co-workers[14] have synthesised WS_2 tubes from $W_{18}O_{49}$ rods produced by heating tungsten foil at high voltages under Ar in the

presence of SiO_2. Therefore we have made strong efforts to prepare metal oxide nanoparticles in large yield and constant quality and size.
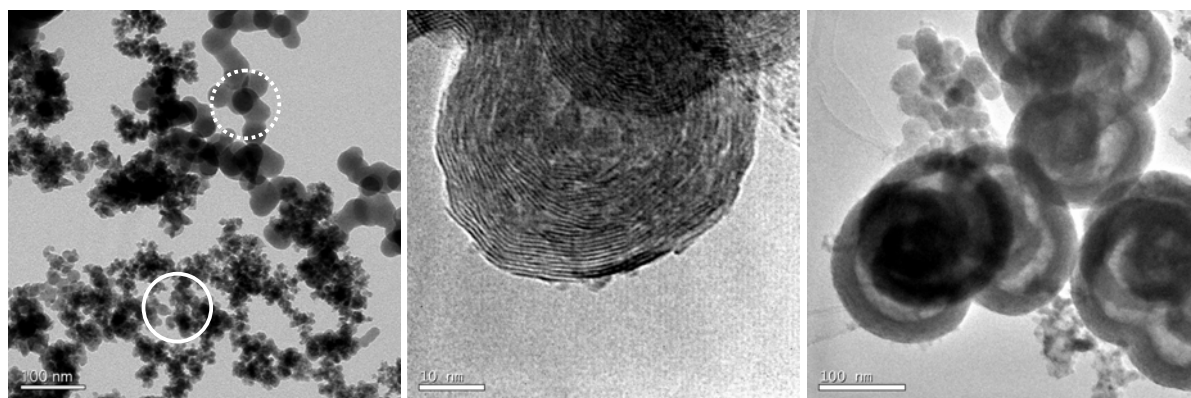

Figure 5. HRTEM micrographs of MoS_2 nanoparticles obtained by MOCVD synthesis at 450°C (a) and subsequent heating on a TEM-heating stage to 700°C (b,c) .

WO_3·nanorods were synthesized in large yield by hydrothermal synthesis starting from tungstic acid, hexadecyl amine as a template and citric acid as a modifier. Synthesis of WO_3 nanorods was also carried out using hydrochloric acid instead of citric acid, while maintaining the pH similar to the reaction which yielded WO_3 nanorods. This reaction resulted in a product containing a mixture of longer rods with variable thickness and unevenly shaped crystalline particles. Similarly synthesis carried out for m < 1 and w < 5 resulted in a mixed product with more highly crystalline WO_3 particles and few bunch-like WO_3 particles. The role of citric acid as a structural modifier and the mechanism involved in the growth of WO_3 is not clear. However, it can be inferred that the amount of citric acid plays an important role in the formation of WO_3 nanorods. One could speculate that at higher m values, the three carboxylate groups of each citric acid could bind to more than one WO_6 octahedron and helping in the olation of WO_6 in a directed manner while hindering the oxolation in all directions due to steric effects. This could lead to the formation of shorter and thinner rods. On the other hand at lower m values, two or more oxygens of the WO_6 octahedra could be contributed from a single citric acid molecule, hence hindering both the olation and oxolation to a large extent. During hydrothermal reaction at 180° C, when citric acid decomposes the hydrophobic hexadecyl amine template could be helping in preserving the rod like structure of the tungsten oxides. For w values > 5 the surface coverage of the growing WO_3 nanorods is not sufficient to limit the particle growth and WO_3 bunches and rods are obtained. When citric acid is fully replaced by hydrochloric acid condensation of WO_6 takes place rather very quickly resulting in a mixture of longer and thicker rods and crystals.

Representative TEM images of the tungsten oxide samples obtained from two different trials of hydrothermal reactions are given in Figure 1 (with m and w given in the caption of Figure 6). Figure 6a shows a part of a WO_3 particle with many non- separable rods protruding out. TEM image of these rods are shown at a slightly higher magnification in the inset of Figure 6a. This sample consists of particles exclusively grown in a bunch-like fashion. Figure 6b shows very well separated WO_3 nanorods aggregated together due to the high surface energy owing to their nanosize. The nanorod lengths in Figure 6b range from 150 to 250 nm and their diameters vary from 5 to 50 nm. A calculation of the particle size distribution of these samples shows that more than 85 % of the tungsten oxide rods are within the range of 15 - 50 nm in diameter.
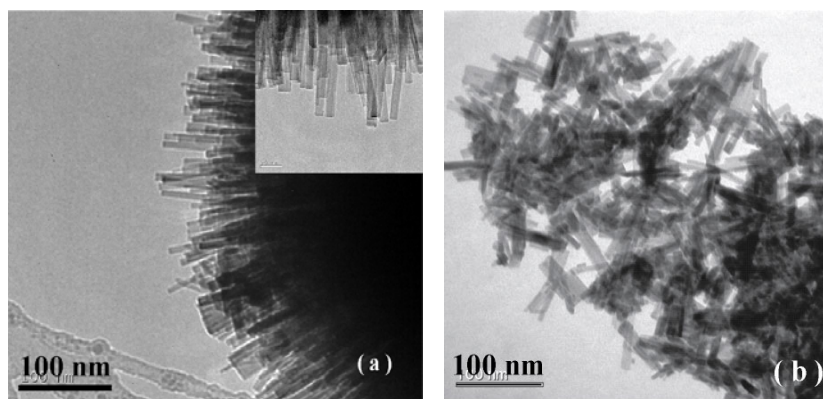
Figure 6. TEM images of WO_3 nanorods synthesized by hydrothermal reactions at different mole percentages m = $\dfrac{[W]}{[A]+[W]+[HDA]}$ [%] or ratios of w = [W]/[HAD] [%] ([W], [A] , and [HAD] correspond to the number of moles of ammonium tungstate, citric acid and hexadecylamine). Figure (a) depicts the bunch- like morphology of the WO_3 particle grown at m = 3.42 and w = 18.6, whereas Figure (b) shows the morphology of WO_3 rods obtained at grown at m = 1.8 and w = 1.6. The WO_3 rods are shown at higher magnification in the inset. w values < 5% and m values $\geq$ 1 resulted in the formation of nanorods.

Figure 7 shows experimental and simulated HRTEM images and SAED diffraction patterns of a WO_3 nanorod. The lattice parameters of 0.38 nm and 0.63 nm correspond to the d-spacings of (001) and (100) of the WO_3 hexagonal cell. These values are also in agreement with the lattice parameters obtained from the powder XRD pattern. All rods tend to grow along the `c´ direction. The high resolution image filtered via FFT with DM3.6 (see inset a) is in good agreement with the image of zone [010] (see inset b) simulated by multi-slice method (thickness of 37 Å, defocus -855 Å, C_s=1.2 mm). The same holds for the dynamically calculated diffraction pattern compared with the experimental SAED pattern. Selected area energy dispersive X-ray analyses (EDX) of individual nanorods exhibit the existence of tungsten and oxygen in an atomic ratio of 1:3.

The nanorods were converted to WS_2 nanotubes by heating the WO_3 nanorods in Ar gas up to 840 °C and then treating them in hydrogen disulphide atmosphere for 30 min. TEM images of WS_2 nanotubes obtained after H_2S reduction (Figure 8a) show the high yield of WS_2 nanotubes. However a manyfold increase in the diameter and the length of the WS_2 tubes compared to the WO_3 starting material was observed. The nanotube thicknesses range broadly from 20 nm -200 nm and their length varies approximately from 1µm to 8 µm. A large fraction of the nanotubes has open ends (Figure 8b). Studies on these nanotubes by HRTEM combined with EDX analyses reveal the complete conversion of oxide rods to sulphide tubes during the reduction process which allows the synthesis of large amounts of multiwalled nanotubes (MWNTs). A HRTEM image of one such representative MWNT is shown in Figure 8c. The interlayer spacing of 0.65 nm between the tubular walls is consistent with the (002) d-spacing of $2H-WS_2$ lattice. The helicity of the nanotube (Figure 8c) could be calculated as ~ 10° based on the Selected Area Diffraction (SAED) pattern (Figure 8d) of the multiwalled WS_2 nanotube.[15]
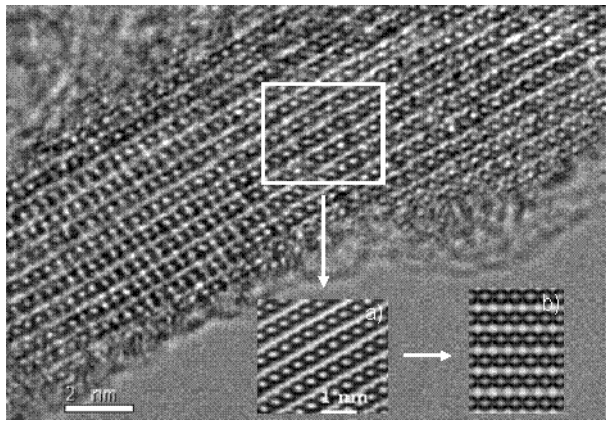
Figure 7. Experimental HRTEM image of a WoO₃ nanorod along b axis (top); the filtered image is shown as inset (a) the corresponding simulated image as inset (b) together with experimental SAED pattern (bottom, left hand side) and dynamically calculated ED pattern for zone [010] (bottom, right hand side).
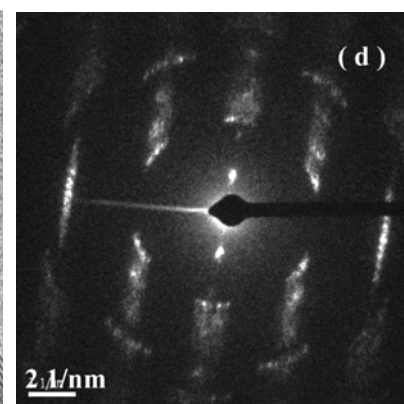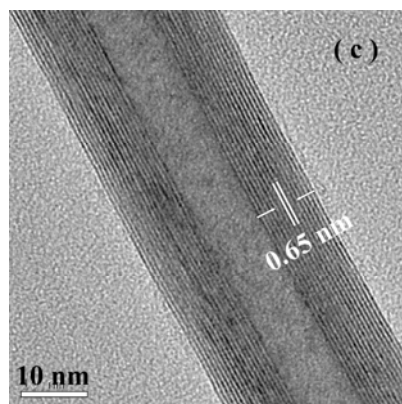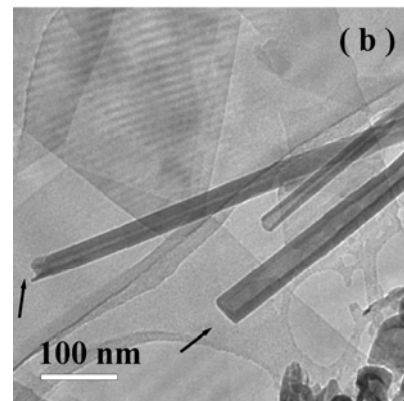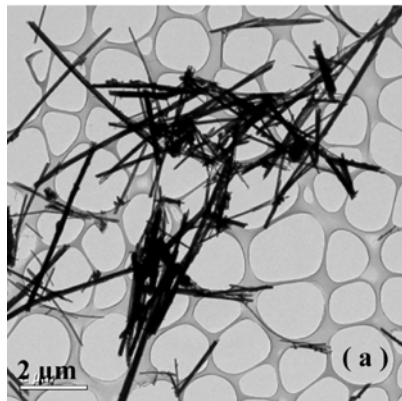

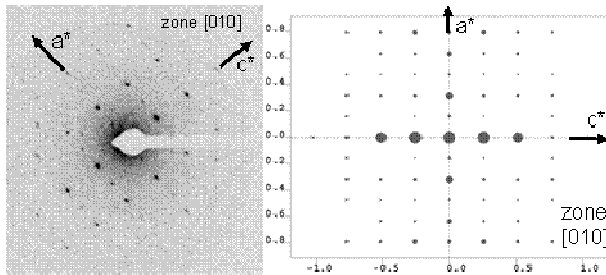**Figure 8.** A low resolution TEM image of the WS₂ nanotubes (a) indicates the yield of nanotubes during the conversion process. TEM image of hollow WS₂ nanotubes (b). The sheet-like appearance in (b) are due to Moire patterns. The open end of a nanotube is indicated by an arrow. HRTEM micrograph of a typical MWNT (c) along with its SAED pattern (d). The chiral angle of the nanotubes could be calculated as ~10° based on the SAED.

Reductive sulfidization proved to be even a more versatile approach when applied under mild conditions. Recently, Nesper and coworkers reported the synthesis of VO_x nanotubes with intercalated template amines using a hydrothermal approach.[4] A conversion of these preformed oxide nanotubes to their respective sulfide counterparts by preserving the tube-like structures and the intercalated template molecules can be achieved by reductive sulfidisation at 250°C. If he reaction is carried out below 200°C, the reactivity of the precursor tubes is too small, carrying out the reaction at 300°C or higher leads to a collapse of the tube structure. The first synthesis of chalcogenide VS_2 nanotubes with intercalated organic molecules by the sulfidisation of a tube-like VO_x precursor. The starting material for the synthesis of the VS_2 nanotubes (NT-VS_2) reported here were vanadium oxide nanotubes (NT-VO_x, x ~ 2.3), which were synthesized by hydrothermal reaction. A representative low resolution transmission electron microscopic image of NT-VO_x is given in Figure 9a. It shows that the NT-VO_x is the main product; the tubes are 0.5-5 µm long and have an outer diameter between 50 and 150 nm. Upon sulfidisation with H_2S at 225°C, these NT-VO_x converted into VS_2 nanotubes. Scanning electron micrograph (SEM) of a typical NT-VS_2 obtained after sulfidisation, given in Figure 9b, show that the structure and the morphology of VO_x tubes are preserved during the oxide to sulfide conversion. SEM also indicate the high yield of NT-VS_2 obtained by this method. Full conversion to NT-VS_2 was observed for NT-VO_x intercalated with dodecyl amine (C_{12}-amine) but not with hexadecyl amine (C_{16}-amine). Reaction temperatures higher than 250°C lead to a total collapse of the VS_2 tubes.

The sulfidisation of the NT-VO_x produced VS_2 nanotubes is evidenced by the high resolution transmission electron microscopic images (HRTEM) in Figure 9c. All tubes are hollow, most of them are open, ca. 20% exhibit flat caps, making a 90° connection with the boundaries of the cylinder. The flat caps give an additional hint that structure of the NT-VO_x precursor is preserved during the sulfidisation. Although the inner VS_2 layers of the tubes are smooth and almost free of defects, we note that the outermost VS_2 layer is partially incomplete (Figure 9c), and each VS_2 tube is surrounded by a coating of amorphous material. In addition, the outermost VS_2 layer exhibits a number of defects. This could be due to an incomplete reconstruction of the outer shell of the oxide precursor during the sulfidisation step.

Figure 9c and d show high resolution TEM images of a partially and a fully converted VS_2 nanotube with lattice fringes corresponding to a layer separation of approximately 2.8 nm and 1.6 nm respectively, which is significantly larger than the layer separation of 0.57 nm in bulk VS_2. The observed layer spacing corresponds to the separation of the VO_x layers in the starting material, which was determined by the chain length of the template molecules used in the synthesis of NT-VO_x. This indicates that the template layer is partially intact in the VS_2 product. This hypothesis is supported by the IR spectra of NT-VO_x before and after sulfidisation, presented in Figure 10. The IR spectra of alkylamine templated NT-VO_x, given in Figure 10a (C_{16}- amine) and Figure 10b (C_{12}-amine), show strong vibrational bands characteristic of alkyl C-C stretching mode at 2920 cm^{-1} and 2850 cm^{-1}. The vibrational bands characteristic of V-O bond appear at 991cm^{-1}, 791 cm^{-1}, 721 cm^{-1}, 575 cm^{-1} and 480 cm^{-1}. The absorption bands corresponding to V=O stretching and V-O-V deformation modes are shifted to lower frequencies compared to the crystalline V_2O_5.[15, 16] A new band at 721 cm^{-1}, which can be attributed to V-NH_2 vibration, indicates that the amine group of the templates is bound to the vanadium atoms in NT-VO_x. Analyses of the VS_2 nanotube samples obtained after sulfidisation show that the C_{16}-amine intercalated NT-VO_x does not convert fully, as indicated by the characteristic broad V-O band at 990 cm^{-1} and tends to retain part of the intercalated templates, which can be deduced from the

vibrational absorption bands at 2920 cm^{-1} and 2850 cm^{-1} in Figure 10c. On the other hand, complete sulfidisation was achieved when C$_{12}$-amine templated NT-VO$_x$ was reduced, as indicated by the absence of all V-O bands, while retaining part of the templates (see Figure 10d). Furthermore, the results of elemental analyses indicate a partial thermolysis (NH$_3$ loss) of the template during the sulfidisation step.
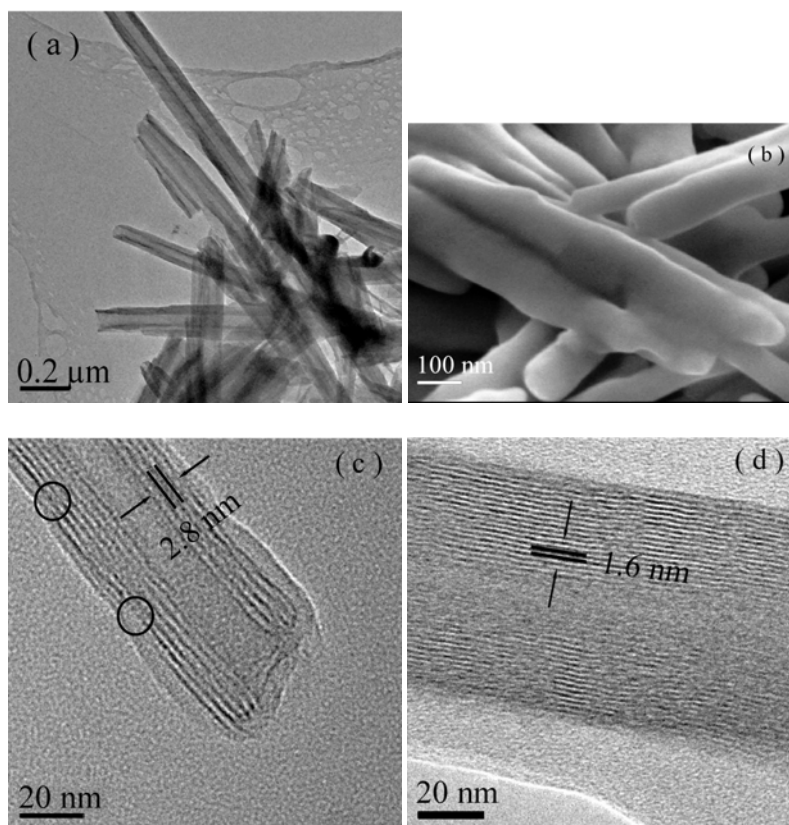

Figure 9. Low resolution overview TEM image of VO$_x$ nanotubes used as a starting material for the synthesis of NT-VS$_2$ (a). Overview SEM image of NT-VS$_2$ obtained after sulfidisation of NT-VO$_x$. (b). HRTEM image of a single VS$_2$ nanotube with a layer separation of 2.8 nm and a flat cap, showing a partially crystalline or amorphous coating (c). Imperfections are marked by a circle. HRTEM of a NT-VS$_2$ obtained from NT-VO$_x$ intercalated with C$_{12}$-amine, with a layer d-spacing of 1.6 nm (d).

In order to ascertain whether the VO$_x$ to VS$_2$ conversion was complete, we performed additional EDX analyses of the products. In Figure 11a we present the EDX spectrum of a partially sulfidised product. The EDX analyses show high sulfur content for the outermost portions of the tube, whereas significant oxygen content is found in the interior part. This result clearly demonstrates that the VO$_x$ nanotubes are converted layer by layer to NT-VS$_2$. Figure 11b shows the EDX spectrum of a VS$_2$ nanotube. The V:S ratio of 1:2 (accuracy $\pm$ 1%) is almost constant over the tube diameter, independent of the beam position. The results indicated that for C$_{12}$-amine intercalated NT-VO$_x$ the conversion is almost complete whereas for C$_{16}$-amine intercalated NT-VO$_x$ the sulfidisation remained incomplete, which is compatible with the IR data presented above.
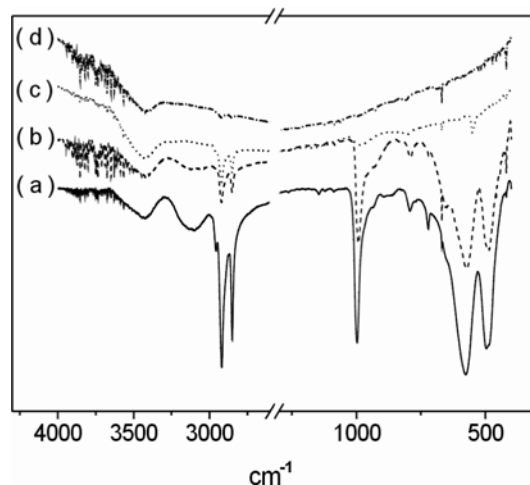
Figure 10. The FT-IR spectra of NT-VO$_x$ samples before and after sulfidisation. (a) NT-VO$_x$ with C$_{16}$-amines (b) NT-VO$_x$ with C$_{12}$- amines before conversion (c) NT-VS$_2$ with C$_{16}$-amines (d) NT-VS$_2$ with C$_{12}$-amines after conversion.
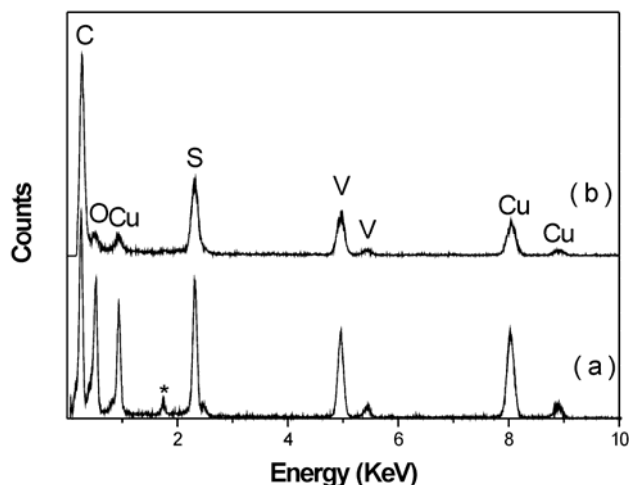

Figure 11. EDX of an isolated hollow VS$_2$ tube, showing the presence of V, O and S signals. Incomplete reaction of C$_{16}$-amine templated nanotube is indicated by the presence of Oxygen in (a) in comparison with (b). Peak marked by * is due to the detector.

Metal Intercalation. Studies on electrochemical intercalation of copper into a partially sulfidised NT-VS$_2$ have revealed that the intercalation of Cu up to a composition Cu$_{0.77}$VS$_2$ can be achieved in NT-VS$_2$. NT-VO$_x$ has been reported to intercalate alkali, alkaline earth and a number of transition transition metals.[17] Studies on copper intercalation of NT-VO$_x$ chemically, by exchanging the intercalated templates with Cu ions in a liquid medium, show that a small fraction (0.08 moles) of copper could be intercalated, with considerable changes in the structure and the morphology of the starting material. In contrast, no electrochemical Cu intercalation was possible in NT-VO$_x$. The discharge / charge voltage profile of Cu intercalation into 4.4mg of NT-VS$_2$ is shown in Figure 12. The voltage of the working electrode dropped gradually until the insertion of Cu up to a limiting composition Cu$_{0.77}$VS$_2$ is reached. This corresponds to a total capacity of 360 mAhg^{-1}. The Cu is reversibly deintercalated in the subsequent oxidation to regain a nominal composition

of VS_2. The next reduction follows the first one, although some irreversibility occurs. The reversible Cu capacity corresponds to a specific capacity of 314 mAhg[-1], in comparison to the theoretical capacity of 372 mAhg[-1] for graphite.[19] The reason for the high feasibility of Cu intercalation and high capacity value of NT-VS_2 in comparison with the so far reported non-carbon nanotubes could be due to the defects that form during the conversion of NT-VO_x to NT-VS_2. This is in line with the previous reports where ball milled MoS_2 nanotubes[20] show better storage capacity compared to their untreated (unactivated) starting counterparts.
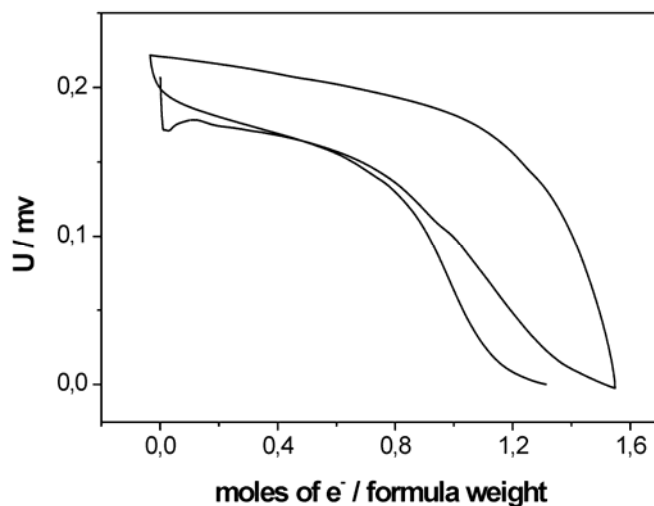

Figure 12: Graph of discharge / charge potential vs the number of moles of electron intercalated per formula weight of NT-VS_2 during Cu intercalation studies is given.

Electronic Structure. Because of their pronounced porosity nanostructured and NT-MoS_2 exhibit a much higher reactivity than crystalline 2H-MoS_2. As a result, Cu can be intercalated electrochemically. Nanostructured MoS_2 shows a reproducible and quasi-reversible intercalation behavior. For typical sample sizes of approx. 20 mg and electrode surfaces of 0.5-1 cm^2 currents of 200 μA could be used for the intercalation without significant variations in the potential curves. These findings are compatible with a good mobility of the guest ions in the host structure. The maximum charge transfer of 0.8 e$^-$ / formula unit is compatible with a composition $Cu_{0.4}MoS_2$. Control experiments with bulk MoS_2 revealed that under identical conditions crystalline 2H-MoS_2 does not intercalate Cu. The results of resistivity measurements on IF-MoS_2 indicate semiconducting behaviour, with resistivity values of 12 kΩcm at room temperature. From the temperature dependence of the resistance we derive a band gap of $E_g \approx 0.1$ eV; the Cu intercalated sample, however shows thermally activated conductivity. EDX studies (line scans) indicate that – in agreement with the picture of a Cu intercalation between the MoS_2 layers Cu is distributed homogeneously in the sample.

Physical Properties of chalcogenide nanotubes

In comparison to the carbon systems - the properties of inorganic nanotubes have been studied only to a limited extent. Optical studies in the UV-vis range and Raman investigations have given some insight into the electronic structure of these systems. This study reports for the first time about spatially resolved two-photon photoemission from NT-MoS_2. A novel approach of energy-filtered imaging utilizing the time-of-flight technique in combination with a fs laser source was used for the spectro-microscopic study of individually

selected nanotubes. The photoemission spectra are compared with calculations for MoS_2 in slab geometry. The imaging time-of-flight technique is described elsewhere. [21] Details of the experimental setup, in particular the photoemission electron microscope (PEEM) and the laser system, are described in [22]. Briefly, the instrument is based on a three-lens electrostatic optics with low column energy additionally equipped with a drift tube and a time-resolving image detector. A frequency doubled Ti:Sapphipe oscillator (Spectra Physics) with a photon energy of 3.1 eV and a fluence of 6.4 $\mu J \cdot cm^{-2}$ served as excitation source.

MoS$_2$ nanotubes were synthesized using silica nanotubes as template. $(NH_4)_2MoS_4$ in dimethyl formamide was heated with the templates under constant stirring, dried, and reduced in a H_2/N_2 gas stream at 450°C Finally, the template was dissolved in HF. A TEM image of one of NT-MoS_2 is shown in the insert to Figure 13. The line scan of the EDX signal that the nanotubes are hollow cylinders with 30-40nm wall thickness, an inner diameter of 120 nm and a length of several micrometers.
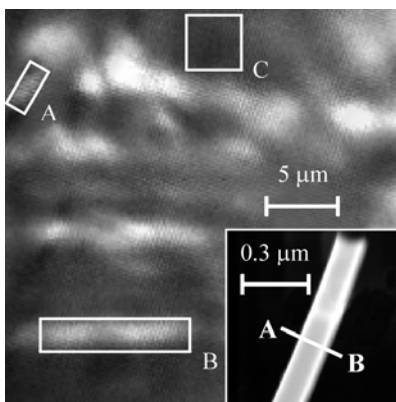

Figure 13. 1: PEEM image of a group of MoS$_2$ nanotubes on SiO$_x$ excited by fs-laser radiation with 3.1 eV photon energy. Insert: TEM image of a nanotube.

The study of chemical composition of a separate nanotube was carried out with the help of the energy dispersive X-ray (EDX) implemented in the transmission microscope. For these measurements, the electron beam was focused on the sample in a region with a lateral size of 1 nm. The region, from which X-ray radiation was analyzed, was somewhat larger (it increases as the sample thickness increases, in the present case as the nanotube wall thickness increases). The EDX analysis reveals the signal from the nanotube constituents Mo and S. The energy resolution (100 eV) did not allow to distinguish the signal coming from Mo L_α (2.293 keV) and S K_α (2.307 eV) edges. The peak at about 17,5 keV is a signal from Mo K_α edge (17.479 keV). The MoS$_2$ nanotubes were dissolved in ethanol and deposited on the smooth surface of a Si-wafer covered by native oxide (SiO$_x$ surface). The coverage was chosen to be low enough that individual nanotubes could be identified and localized in the PEEM images.

Figure 14 (a-c) show spectra extracted from different regions (A: small NT, B: large NT, C: substrate) of the sample as marked in Figure 13. The energy scale of the spectra is referenced to the top of the valence band becoming visible at an energy of about 6.2 eV (i.e. 2*hv)*. The local work function of the micro areas results in a different low-energy cut off of the spectra. The work function of the substrate is determined to be 4.0 eV, whereas the value of the nanotube(spectra a, b) is lower by $\Delta\Phi$ = 0.3 eV. The NT spectra show a width of 2.5 eV, thus allowing to study the topmost region of the valence states. The Si-spectrum (c)

(weighted by an empirical scaling factor) was subtracted from the NT spectrum (b) to account for the background emerging from the Si substrate. The result is shown as spectrum (d).
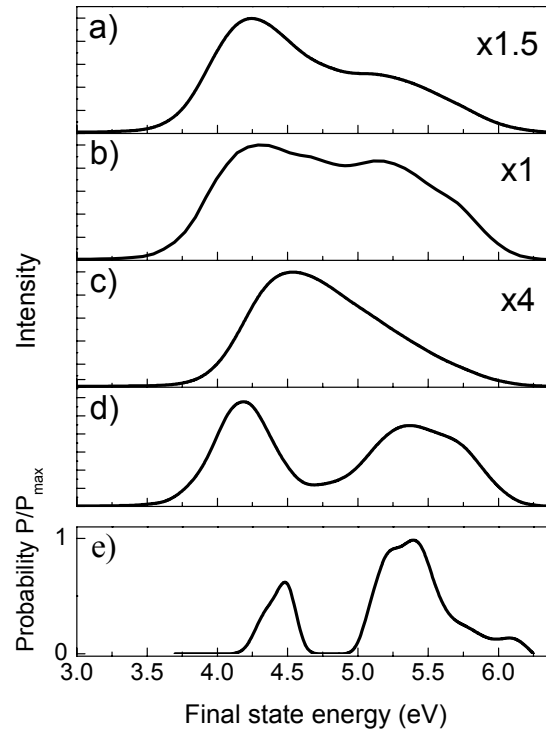

Figure 14. Local spectra of selected nanotubes (a, b, corresponding to regions A and B in Figure 13) and the Si substrate (c, region C in Figure 13). Spectrum (b) after background correction is shown in (d). The probability for direct transitions (e) at the excitation with 3.1eV photons was derived from the calculated density of states.

Electronic structure calculations were performed in order to explain peculiarities of the spectra. The limiting case of a nanotube with infinite diameter is a single slab, therefore slab calculations were used to estimate the electronic structure of the nanotubes. Bulk MoS_2 exhibits already a layer type structure and it showed up that the difference in the density of states (DOS) between slabs and bulk material is also not very pronounced. The results of the calculation are shown in Figure 15. The calculation reveals the slabs to be semiconducting with a band gap of about 1 eV, being comparable to bulk material. The band structure may not be directly comparable to a NT as this has 1-dimensional symmetry whereas the slab has 2-dimensional symmetry. In the limit of large diameter tubes, however, the DOS should be comparable. It may also be better for comparison with the observed spectra, as it is already an integrated quantity. One possible two-photon transition is indicated in Figure 15 by arrows. The DOS exhibits a pronounced maximum at about 1 eV below the valence band maximum (E_{VB-max}). The maximum in the unoccupied DOS at about 2 eV will serve as a very effective intermediate state for the two-photon process such that a coherent excitation is possible. This leads to much higher intensities compared to two-photon transitions through virtual intermediate states as often observed in metals with a very low DOS in the unoccupied part of their band structures (e.g. Cu or Ag).
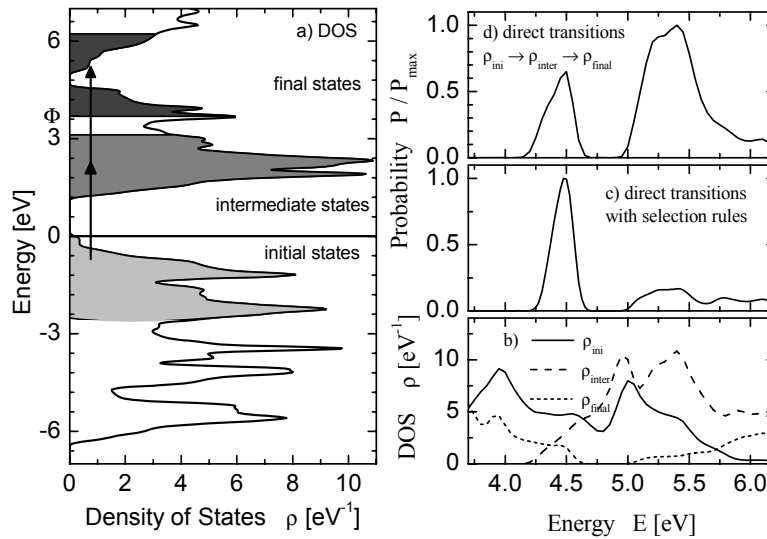
Figure 15. Calculated density of states (a) of a MoS$_2$ slab. The arrows denote one possible two-photon transition. Φ denotes the experimental work function. The shaded areas assign the ranges that are energetically allowed to take part in the two-photon excitation. b) shows the DOS-parts being relevant for direct photo-excitation on a shifted energy scale and c), d) the corresponding probability (see text).

Due to the gap in the intermediate DOS, there are no direct transitions possible into states below 4.2eV final state energy. The gap in the final state DOS prevents direct transitions into states between 4.7eV and 5.2eV. The probability for direct transitions may be estimated from a convolution of the DOS in the initial, intermediate, and final states (Figure 15b) and neglecting the transition matrix elements. From the probability in Figure 15d, it is seen that high intensities are expected at final state energies of 4.5eV and in the range of 5.2eV to 5.4eV. The high density in the intermediate DOS (1.8eV to 2.3eV above E_{VB-max}) may also serve very effectively as base for high intense indirect transitions at 5.4eV. The dipole selection rules, in particular $\Delta l = \pm 1$, will give an additional weighting factor for the expected intensities as is seen from Figure 15d. The high probability for transitions at about 4eV is governed by a $p \rightarrow d \rightarrow p$ transition. In the energy range from 5eV to 5.5eV the excitation of p and d valence electrons has nearly equal probability. It should be mentioned, however, that the non-linear excitation may not be described completely by the dipole selection rules.

The calculated probability of the direct transitions reproduce the measured spectra reasonably well, in particular the gap in the final states is reproduced. The energetic positions of the maxima at 5.25eV and 5.75eV are slightly shifted towards the high energy cut off, what may arise from the underlaying indirect transitions or the influence of the substrate on the nanotube, compared to a free single nanotube. The substrate spectrum exhibits no structures at these energies (Figure 15c), thus the observed features have to originate from the nanotubes. The nanotubes in regions A and B of Figure 14 have different sizes and their spectra, in particular the height of the low-energy peak is different. This peak contains the contribution of secondary electrons as well as the transitions to the low-energy peak (4.5 eV) of the probability for direct transitions.

Functionalization of oxide and chalcogenide nanoparticles and -tubes.

The nanoengineering of particle surfaces is a key for the design and tailored construction of innovative nanomaterials. Having control of the inorganic nanoparticle surfaces allows one to tailor the particle size and solubility. Moreover, the surface characteristics of nanomaterials influence the broad range of properties and the performance of a large variety of devices. To connect the inorganic nanomaterials to the organic moiety in hybrid materials by strong covalent or ionic interactions, reactive organic groups have to be attached on the surface of inorganic component. Surface modification of nanomaterials can be achieved either grafting of organic groups to the surface of nanomaterials after synthesis (post-functionalization) or by *in situ* modification of nanomaterials by organic compounds (*in situ*-functionalization). The surface of metal oxide particles can be functionalized in a straightforward manner. The surface chemistry of chalcogenides is more difficult to tackle. Whereas simple sulfides such as CdS are still amenable to complexation, layered chalcogenides are much more inert because of the sulfur lone pairs pointing away from the surfaces, while the metal is sandwiched by the chalcogen layeres and therefore hardly accessible for complexation by any ligands. Here we show how metal oxide particles can be functionalized by a very versatile polymeric ligand which can be used for *in-situ - and post-functionalization* of TiO_2 as well as for other metal oxide nanomaterials.[23] An entry to the surface chemistry of layered chalcogenides can be achieved with the aid of metals whose coordination sphere is sheathed by a group of tripod ligands.

The multifunctional polymeric ligand used for the surface functionalization of TiO_2 as a typical representative of metal oxides combines three properties: (i) a robust anchor group based on dopamine, capable of binding to many metaloxides (TiO_2, Fe_2O_3, etc.),[24] (ii) a functional molecule (fluorescent dye, catalysts, biological molecules, etc.), and (iii) an outer group to provide solubility in different solvents, thereby allowing to tune the application of the inorganic nanomaterials (e.g. solubility of TiO_2 pigments, directed binding to biological targets etc.). The architecture of the polymeric ligand is of major importance, because it provides the basis of a comprehensive toolbox to construct supramolecular assemblies of organic-inorganic hybrid nanomaterials. Moreover, this strategy of functionalization can be extended by introducing suitable anchor groups for nanomaterials other than metal oxides.[25]

The fact that active ester polymers react fast and quantitatively with amines to form the corresponding poly(acrylamides), opens the possibility to obtain multifunctional polymeric materials. Active ester polymers based on pentafluorophenylacrylates exhibit some outstanding features compared to the commonly used poly (N-hydroxysuccinimide-acrylates): better solubility and higher reactivity, as described elsewhere.[26] Polymers **P1, P2,** and **P3** exhibit three different properties: (i) a fluorescent dye as a functional demonstrator molecule (ii) 3-hydroxytyramine as anchor groups for attachment onto the metal oxide nanoparticles and (iii) a long alkyl chain to increase solubility in nonpolar solvents.

For the *in-situ* functionalization of the TiO_2 nanocrystals, $TiCl_4$ was injected into the solution of the polymeric ligand in benzyl alcohol. The solution was stirred for two days at 80°C under argon atmosphere. Post-functionalization was achieved by sealing a mixture of TiO_2 nanowires (synthesized from conc. NaOH and titanium isopropoxide) and 10 ml of polymeric ligand in benzyl alcohol. In both cases the product was repeatedly washed with CH_2Cl_2 to remove the unreacted ligand. The functionalized TiO_2 nanocrystals were

characterized by TEM, XRD, ^{1}H-NMR, confocal laser scanning microscopy (CLSM) and fluorescence spectrophotometry.
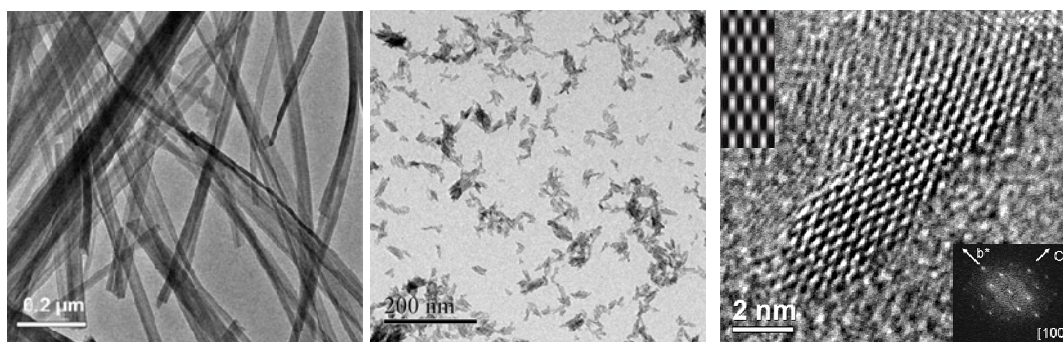

Figure 16. Transmission electron micrographs of (a) synthesized TiO$_2$ nanowires, (b) nanoparticles (overview image) and (c) HRTEM image of an individual nanoparticle. The Fourier Transform (FFT) is given in the lower right corner. A theoretical HRTEM image of the [100] zone is shown given in the upper left corner.
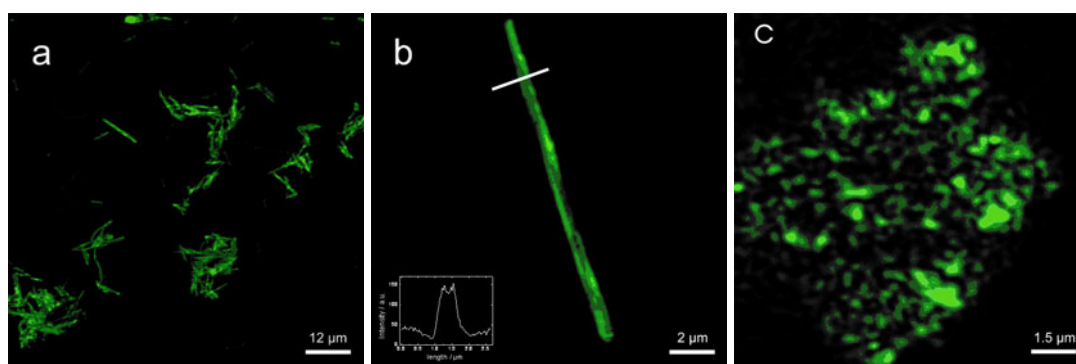

Figure 17. Confocal Laser Scanning Microscopy images of TiO$_2$-nanowires (a-d) and *in situ*-functionalized nanoparticles (e and f). TiO$_2$ nanowires coated with **P2** (NBD, a and b), and TiO$_2$ nanoparticles *in situ*-functionalized with **P2** (NBD, e). The fluorescence profiles for post-functionalized TiO$_2$ nanowires are given in the inset of b.

Transmission electron micrographs of synthesized TiO$_2$ nanowires and TiO$_2$ nanoparticles are shown in Figure 16. An overview of the nanowires is given in Figure 16a. These nanowires have been used for post-functionalization. Figure 16b and 16c show the TEM images of the *in situ* synthesized functionalized TiO$_2$ nanoparticles (using the fluorescent dyes 1-pyrenemethylamine (**P1)**, piperazinyl-4-chloro-7-nitrobenzofurazane (**P2)** and Texas Red (**P3**) at low magnification as well as at high resolution, respectively. At low magnification (Figure 16b) it can be seen that the sample consists almost exclusively of nanometer-sized TiO$_2$ particles arranged in a partly agglomerated fashion on a TEM grid. Even though it is difficult to identify isolated, individual TiO$_2$ particles because of the presence of the polymeric ligand, a HRTEM image of an isolated particle is shown in Figure 16c. XRD and TEM (see inset of Figure 16c), reveal the characteristic diffraction patterns of anatase. The theoretical HRTEM image of the [100] zone (given in the upper left corner) has been calculated by a multi-slice method for a thickness of 2 nm at Scherzer focus and resembles the experimentally derived image nicely. The crystallinity and the morphology of the TiO$_2$ nanoparticles are independent of the polymeric ligand **P1**, **P2,** or **P3** used in the syntheses. Figure 17 shows the confocal laser scanning microscopy images of TiO$_2$ nanowires and nanoparticles after surface functionalization with **P2**. A 10 μl droplet of the

sample was placed and dispersed carefully on a thin glass slide and the solvent was evaporated. **P2**-functionalized nanowires and nanoparticles were imaged using an argon laser with an excitation wavelength of 488 nm. A 40x (NA 1.25) oil immersion objective was used for the imaging of all samples.

Overview images of as functionalized TiO_2 nanowires with the polymeric ligand **P2** are shown in Figure 17 (a and c), while a single isolated nanowire can be seen in Figure 17b. It is obvious from the fluorescence profiles (given in the inset of Figure 17c and images that the nanowires are fully coated by polymer ligands covalently bound to TiO_2 nanowires. It is difficult to comment on the actual size of the *in-situ* functionalized nanoparticles because it was beyond the resolution limits of CLSM. TiO_2 nanocrystals with surface bound dopamine have been used for biotin-avidin functionalization coupling. Dopamine binding is a standard method for the surface functionalization of metal oxides where the dopamine group preferentially binds to the edges of the TiO_2 nanocrystals (which have a higher surface energy). In contrast, full surface coverage, protection and concomitant functionalization can be achieved using the novel copolymer ligand containing a large number of dopamine groups covalently linked to the polymer backbone where the nanoparticles are partly sheathed by surface bound anchor groups and partly by steric shielding through the polymer ligand.
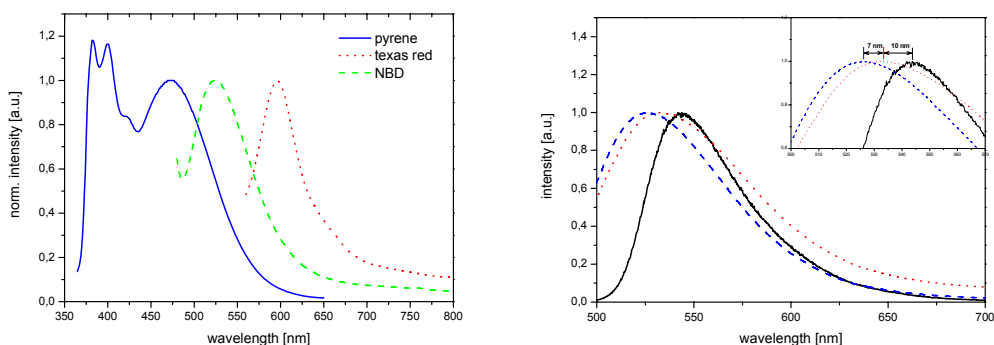

Figure 18. (a) Fluorescence spectra of TiO_2 nanoparticles coated with **P1** (pyrene, solid line), **P2** (NBD, dashed line) or **P3** (Texas red, dotted line). TiO_2 nanoparticles carrying the **P1** pyrene fluorophore were excited at 345 nm. TiO_2 nanoparticles coated with **P2** were excited at 460 nm, and the fluorescent spectra for **P3** were recorded with an excitation wavelength of 488 nm. (b) Fluorescence spectra of NBD depending on the preparation conditions. Solid line; emission spectrum of **P2** dissolved in $CHCl_3$, TiO_2 particles coated with **P2** show a 10 nm blue-shifted maximum, whereas TiO_2 particles with the polymeric ligands (**P2**) show a blue shift of 17 nm with respect to **P2**.

The versatile use of the functional polymeric ligands as an immobilizer for metal oxide nanowires and nanoparticles is demonstrated by the attachment of three different fluorescent dyes: pyrene (**P1**), NBD (**P2**) and Texas Red (**P3**), respectively. In order to detect the immobilization of the functional polymers on the TiO_2 surfaces, fluorescence spectra have been measured. Figure 20a shows the fluorescence spectra of TiO_2 nanoparticles coated with **P1** (solid line), **P2** (dashed line) or **P3** (dotted line). All samples were dissolved in $CHCl_3$ for emission spectroscopy. TiO_2 nanoparticles carrying the **P1** pyrene fluorophore were excited at 345 nm. TiO_2 nanoparticles coated with **P2** were excited at 460 nm, and the fluorescent spectra for **P3** were recorded with an excitation wavelength

of 488 nm. Clearly, the expected emission spectra of the respective dye can be seen, proving the flexible application of our functional polymeric ligands.

The functional polymeric ligands have been used for post- and *in-situ*-functionalization of TiO_2 nanoparticles. Therefore, we investigated the fluorescence of **P2** depending on the synthetic procedure. The results are summarized in Figure 18b. The solid line in Figure 18 shows the emission spectrum of **P2** dissolved in $CHCl_3$ as a reference. TiO_2 nanowires which have been coated with **P2** show a fluorescent spectrum with a 10 nm blue-shifted maximum whereas TiO_2 nanoparticles which were synthesized using the polymeric ligand (**P2**) show a blue shift of 17 nm with respect to **P2** in emission maximum. This can be understood as follows. The nanoparticles are coated with the polymer which results in a non-uniform environment for the dye molecules. As a result, the hydrophilic TiO_2 surface induces a slight blue-shift. This also explains the larger blue-shift for the *in situ*-functionalized nanoparticles as compared to post-functionalized nanowires, as the nanoparticles exhibit a larger surface-to-volume ratio.
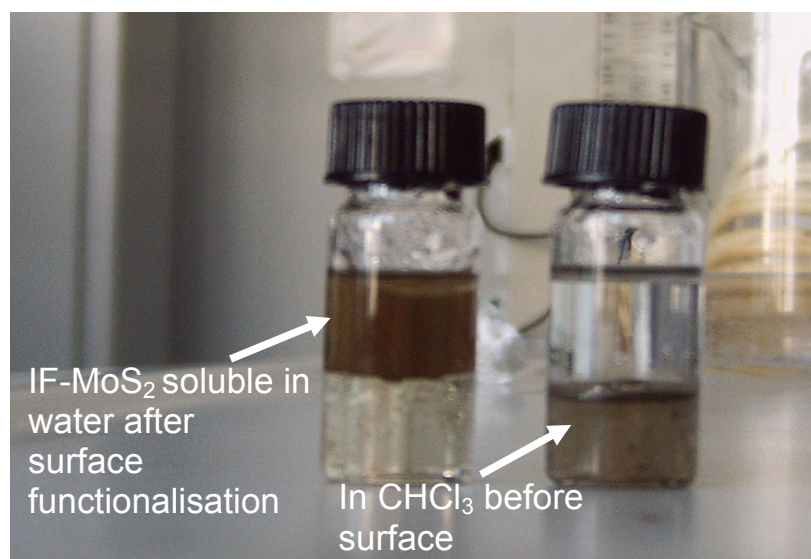

Figure 19. Solubility of IF-MoS$_2$ in aqueous or non-aqueous solvents after surface functionalization.

In conclusion, we have demonstrated for the first time that reactive polymer ligands containing dopamine serve as robust anchor on the surface of metal oxide nanoparticles. Compared to the binding of molecules to the surface of oxide particles using dopamine the novelty and superiority of the polymeric ligand system presented here is based on its multifunctionality, as it incorporates metal chelating ligands, a functional molecule (pyrene, NBD, and Texas Red) and additional entities which allow tailoring the solubility of inorganic nanocrystals in different organic solvents for various potential applications. A possible extension of the work presented we envisage functionalization of chalcogenide nanotubes using nitrilotriacetic acid (NTA) coordinated to Ni^{2+} as an anchor ligand. As an example we show the solubilization of IF-MoS$_2$ nanoparticles in Figure 19. This simple strategy should provide also a useful way to link biofunctional molecules in almost any solvent to the surface of metal oxide/chalcogenide nanoparticles, which may have a high affinity to dopamine or any other linker group which may replace the dopamine ligand in the polymer. This strategy is extremely versatile and offers new opportunities for optoelectronic and/or biological applications of metal oxide nanoparticles. Finally, this strategy allows the

arrangement of inorganic nanoparticles to build up supramolecular structures, e.g. by introducing biotin/streptavidin linker units as functional molecules.

References

[1] J. Cumings, A. Zettl, *Chem. Phys. Lett*. **2000**, *316*, 211

[2] R. Tenne, *Chem. Eur. J*. **2002**, *8*, 5297.

[3] Y. Rosenfeld Hacohen, R. Popovitz-Biro, Yehiam Prior, S. Gemming, G. Seifert and R. Tenne, Phys. Chem. Chem. Phys., 2003, 5, 1644.

[4] M.E. Spahr, P. Bitterli, R. Nesper, F. Krumeich, H.U. Nissen *Angew. Chem*. Int. Ed. **1998**, *37*, 1263.

[5] R. Tenne, L. Margulis, M. Genut, G. Hodes, *Nature* **1992**, *360*, 444.

[6] Y. Feldman, E. Wasserman, D. J. Srolovitz and R. Tenne, *Science* **1995**, *267*, 222.

[7] O. Stéphan, Y. Bando, A. Loiseau, F. Willaime, N. Shramchenko, T. Tamiya, T. Sato, *Appl. Phys. A* **1998**, *67*, 107.

[8] R. Sen, A. Govindaraj, K. Suenaga, S. Suzuki, H. Kataura, S. Iijima, Y. Achiba, *Chem. Phys. Lett.* **2001**, *340*, 242.

[9] D. Vollath, D. V. Szabó, *Acta Mater*. **2000**, *48*, 953.

[10] N. Sano, H. Wang, M. Chhowalla, I. Alexandrou, G. A. J. Amaratunga, M. Naito, T. Kanki, *Chem. Phys. Lett*. **2003**, *368*, 331.

[11] P. A. Parilla, A. C. Dillon, K. M. Jones, G. Riker, D. L. Schulz, D. S. Ginley, M. J. Heben, *Nature* **1999**, *397*, 114.

[12] C. Schuffenhauer, R. Popovitz-Biro, R. Tenne, *J. Mater. Chem*. **2002**, *12*, 1587.

[13] A. Zak, Y. Feldman, V. Alperovich, R. Rosentsveig, R. Tenne, *J. Am. Chem. Soc*. **2000**, *122*, 11108.

[14] Y. Q. Zhu., W. K. Hsu, N. Grobert, B. H. Chang, M. Terrones, H. Terrones, H. W. Kroto D. R. M. Walton, *Chem. Mater*. **2000**, *12* , 1190.

[15] R. Rosentsveig, A. Margolin, Y. Feldman, R. Popovitz-Biro, R. Tenne, *Appl. Phy.* **2002**, *A74*, 367.

[16] J. M. Reinoso, H.-J. Muhr, F. Krumeich, F. Bieri, R. Nesper, *Helv. Chim. Acta* **2000**, *83*, 1724.

[19] B. Gao, A. Kleinhammes, X. P. Tang, C. Bower, L. Fleming, Y. Wu, O. Zhou, *Chem. Phys. Lett.* **1999**, *307*, 153.

[20] J. Chen, N. Kuriyama, H. Yuan, H. T. Takeshita, T. Sakai, *J. Am. Chem. Soc.* **2001**, *123*, 11813.

[21] G. Schoenhense, A. Oelsner, O. Schmidt, G. H. Fecher, V. Mergel, O. Jagutzki, and H. Schmidt-Boecking, *Surf. Sci*. **2001**, *480*, 180.

[22] A. Chinchetti, A. Oelsner, G.H. Fecher, H.J. Elmers, G. Schönhense *Appl. Phys. Lett*. **2003**, *83***,** 1503 .

[23] J. L. Dalsin, L. Lin, S. Tosatti, J. Vörös, M. Textor, P. B. Messersmith, *Langmuir* **2005**, *21*, 640.

[24] N. M. Dimitrijevic, Z. V. Saponjic, B. M. Rabatic, and T. Rajh, *J. Am. Chem. Soc*. **2005**, *127*, 1344.

[25] I. Potavova, R. Mruk, S. Prehl, R. Zentel, T. Basche, A. Mews, *J. Am. Chem. Soc*. **2003**, *125*, 320.

[26] M. Eberhardt, R. Mruk, P. Theato, R. Zentel, *Europ. Polym. J*. **2005**, *41*, 1569.